Plasma Physics and Controlled Fusion

Pedestal analysis of MAST ELMy regimes

To cite this article: S F Smith *et al* 2022 *Plasma Phys. Control. Fusion* **64** 045024

OPEN ACCESS
IOP Publishing
Plasma Physics and Controlled Fusion
Plasma Phys. Control. Fusion **64** (2022) 045024 (15pp)
https://doi.org/10.1088/1361-6587/ac529b

Pedestal analysis of MAST ELMy regimes

S F Smith[1],*, A Kirk[1], B Chapman-Oplopoiou[1], J G Clark[1,2], C J Ham[1], L Horvath[1], C F Maggi[1], R Scannell[1], S Saarelma[1] and the MAST Team

[1] UKAEA-CCFE, Culham Science Centre, Abingdon, Oxon, United Kingdom
[2] Department of Electrical Engineering and Electronics, University of Liverpool, Liverpool L69 3GJ, United Kingdom

E-mail: sfsmith509@gmail.com

Received 8 December 2021, revised 21 January 2022
Accepted for publication 7 February 2022
Published 15 March 2022

Abstract

Mega Ampere Spherical Tokamak (MAST) pedestal data has been analysed, where a pedestal database of 892 shots was obtained, using the upgraded MAST Thomson scattering (TS) diagnostic. Various edge localised mode (ELM) types are discussed, where characteristics and trends of MAST pedestals are shown. The data from the upgraded TS diagnostic confirms pedestal characteristics found in earlier analysis, using previous TS systems. Using the database, calculations of the bootstrap current are obtained using the different analytical formulae (Sauter and Redl), and comparisons are performed. The upgraded MAST TS system now spans the full plasma mid-plane, such that direct comparisons between inboard and outboard pedestals can be obtained, and asymmetries in the density pedestal width were found. To increase confidence in spherical tokamak pedestal predictions, the assumptions of Europed have been validated from the MAST pedestal data, and a value for the kinetic ballooning mode constraint ($C \sim 0.145$) has been obtained. The first spherical tokamak pedestal predictions were performed in Europed and compared to experimental values. Using $C = 0.145$ the temperature pedestal height was predicted to within 10% of the experimental value. In addition type II ELMs on MAST are analysed, and stability analysis and parameter scans have been performed using ESSIVE. Similar magneto-hydrodynamic (MHD) stability properties are observed for type I and type II ELMs, originating from the mixed ELM regimes; it is therefore difficult to distinguish these ELMs using the ideal MHD codes.

Keywords: ELMs, MAST, spherical tokamaks, pedestal database analysis, stability analysis, Europed pedestal predictions

(Some figures may appear in colour only in the online journal)

1. Introduction

Currently, the favoured operating regime for a tokamak is the high confinement mode (H-mode) [1], where increased core plasma pressure is encouraging but edge localised mode (ELM) instabilities occur. Filaments are ejected from the plasma when an ELM occurs [2] transporting energy and particles to the divertor region, resulting in a loss in the pedestal energy [3]. Large and uncontrolled type I ELMs on future tokamaks, such as ITER, are predicted to generate high enough heat fluxes to damage machine facing components [4]. It is therefore important to understand the conditions under which type I ELM instabilities occur, and to make reliable pedestal predictions for future devices. Exploration and development of ELM free operational regimes or regimes with small ELMs is also underway [5].

---

* Author to whom any correspondence should be addressed.

1361-6587/22/045024+15$33.00 Printed in the UK

The Mega Ampere Spherical Tokamak (MAST), a low aspect ratio tokamak based at Culham in the UK, operated from 2000 to 2013 and has recently undergone an upgrade to MAST-U [6]. Pedestal data from the final three physics campaigns on MAST, obtained using a 130 point Thomson scattering (TS) diagnostic [7, 8], is analysed here in anticipation of the initial MAST-U pedestal data analysis. The data analysed from this former tokamak can inform spherical tokamak pedestal research, contribute to the understanding of MAST-U pedestal physics, and to the knowledge of pedestal characteristics for future spherical tokamaks, such as STEP [9].

Previous MAST pedestal data has been analysed in [10–12], where a wide range of ELM regimes have been observed. The most common is the type I ELM regime, with type III ELMs also occurring in many discharges, and a branch of the type III ELMs, also referred to as type IV ELMs were found, appearing in low collisionality plasmas [13]. Type II ELMs have also been observed in MAST plasmas [14]. The method for obtaining the MAST pedestal database is described in section 2. In section 3 analysis of the pedestal database is performed and includes an overview of the different ELM types. The data confirms pedestal characteristics found in earlier analysis, using previous TS systems. The upgraded TS system views the entire plasma mid-plane from the high-field-side (HFS) to the low-field-side (LFS). In section 3.2 a direct comparison has been performed between the HFS and LFS data in the lower single null (SN) and connected double null (DN) configurations.

Bootstrap current calculations are performed using the Sauter *et al* [15] and Redl *et al* [16] analytical formulae. Comparisons of the radial peak in the edge bootstrap current density ($j_{BS,peak}$) calculations are given in section 3.3. Calculations of $j_{BS,peak}$ using both formulae have also been performed in the HELENA code [17] and compared to the experimental data.

Accurate pedestal predictions are important for obtaining boundary conditions for core transport simulations, that can predict the plasma performance. Europed [18] can be used for predictions of peeling-ballooning (P-B) limited pedestals. Europed is based on the EPED1 model [19], where the pedestal height and width can be predicted. EPED predictions have been obtained on various conventional tokamaks [20], and more recently predictions for MAST pedestals have been performed [21]. However, it is still important to analyse the MAST data to verify whether the Europed/EPED model assumptions are valid for MAST and spherical tokamaks in general. This is investigated in section 4, where it has been possible to determine Europed input parameters from the experimental database and use these for first spherical tokamak pedestal predictions using Europed.

The type I ELM analysis is useful for investigating the highest confinement regime by finding P-B pedestal limits, but research is also performed for other operating regimes, that could be used in future spherical tokamaks, such as STEP. The type II ELM regime is one such potential operating regime as the global energy confinement can be as high as the type I ELM regime, whilst pedestal energy loss per ELM is low [14]. Type II ELMs are observed in specific circumstances in MAST plasmas [14] and have been observed in highly shaped, high pedestal density plasmas in various tokamaks including JET [22], ASDEX-Upgrade [23, 24] and NSTX [25]. In section 5 MAST type II pedestal characteristics are discussed. Ideal magneto-hydrodynamic (MHD) stability analysis is also performed for the type II ELMs using ESSIVE, and a comparison is made to type I ELMs. Finally, a summary and conclusions are given in section 6.

2. Obtaining the MAST pedestal database

From 2007 to 2013 the final three campaigns took place at MAST, this paper investigates the pedestal characteristics obtained in preparation for the new physics campaigns on MAST-U and to support the development of STEP. The database includes over 800 shots, where an ELMy H-mode has been obtained, in either a lower SN or DN configuration. Typical MAST SN and DN configurations are shown in [12]. In the DN configuration the two x-points are roughly on the same flux surface. From the database, the gap between these surfaces at the outboard mid-plane (δr_{sep}) is no larger than 6.5 mm.

The database contains a range of shots with various plasma parameters, MAST plasmas typically have a major radius of $R \sim 0.85$ m and a minor radius, $a \sim 0.55$ m. The toroidal magnetic field on axis (B_T) ranges from 0.3–0.5 T, the plasma current (I_p) ~0.4–1.0 MA, the Greenwald density ~0.3–0.95, the safety factor at 95% of flux surface $q_{95} \sim 2$–9 and the heating power from neutral beam injection is ~1.0–3.8 MW. The plasma elongation varies from $\kappa \sim 1.4$–2.1 and the average triangularity (i.e. $(\delta = (\delta_u + \delta_l)/2.0)$, from $\delta \sim 0.25$–0.53.

The upgraded TS system [7, 8] on MAST, was used to measure the electron density (n_e) and temperature (T_e) profiles across MAST plasmas. The system uses eight Nd:YAG lasers, each with a repetition rate of 30 Hz. This upgrade enhanced the previous edge Nd:YAG [26] and Ruby TS [27] systems. The Nd:YAG laser is located 14.5 mm above the centre of the machine, with 130 points radially across giving a spatial resolution of ~1 cm. In the SN configuration the laser beams are approximately 30 cm vertically above the magnetic axis of the plasma. In the DN configuration the laser beams are approximately the at the height of the magnetic axis. For comparison between pedestal widths in DN and SN discharges the SN profiles are mapped to the z location of the magnetic axis. The TS system on MAST allows for measurements, at the mid-plane, radially across the whole plasma, allowing for comparisons of the LFS and HFS pedestals in both the SN and DN configurations.

Examples of typical time traces of MAST shots are shown in figure 1. For a visual comparison of the ELM phases, the time axes have been offset for each pulse to approximately the start of the H-mode period, characterised by a drop in the D_α signal. The plasma current, neutral beam power, core electron temperature and line averaged density are given in figures 1(a)–(d) respectively, showing the H-mode period. The D_α trace for a SN discharge is given in figure 1(e), where only type I ELMs are observed. Figure 1(f) shows the D_α trace for a DN discharge where type III ELMs are observed at the start of H-mode, after a transition occurs to type I ELMs. In figure 1(g)

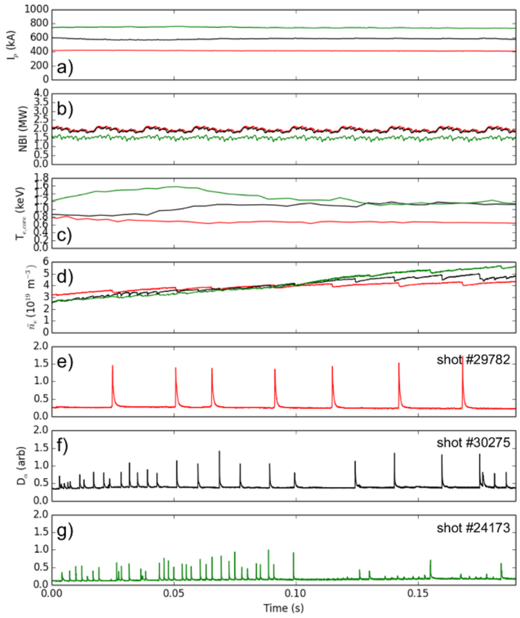

Figure 1. Time traces for three MAST shots, showing the plasma current, neutral beam power, the core temperature, the averaged line density and the D_α traces. The red lines indicate a type I ELM regime in the SN configuration, the black lines show the traces for a DN configuration and the green lines a type II interspersed with type I in a DN configuration.

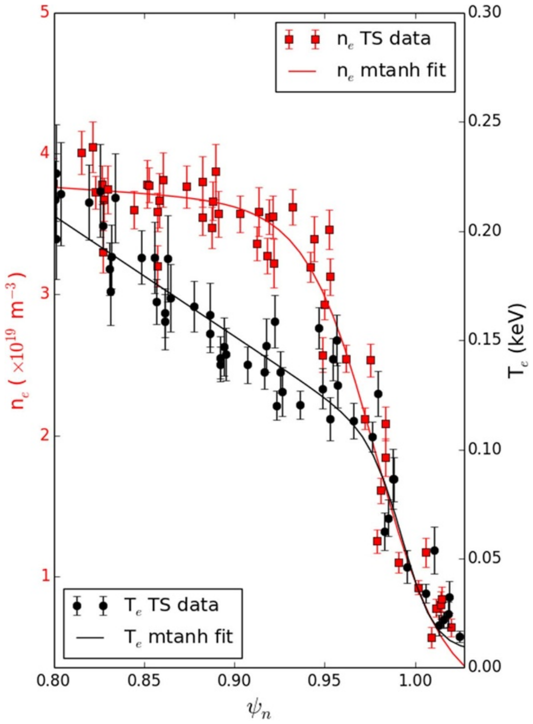

Figure 2. Example of TS profiles for the electron density and temperature. Profiles from shot #29782 have been ELM averaged for the final 25% of the cycle. The ELM averaged data is fitted with an mtanh function and the n_e profile shifted in ψ-space to align with $T_{e,sep} = 40$ eV.

another DN discharge is shown. From ~0.1 s periods of small type II ELMs are observed, these are interspersed with type I ELMs. For the database, MAST H-mode shots were first identified, and then using the D_α trace of a discharge, it was possible to collect the data for the observed ELM-y regime.

When the data is collected the first ELM is neglected, as it is not representative of the following ELMs. Prior to the first ELM a dramatic increase of the edge density, above the central density, is observed [28]. Therefore, the collection of data starts after the first ELM until the last ELM or for the duration of the H-mode. For each TS time point within this period the profile data for n_e and T_e is included in the database. The data points that occur 0.2 ms before and after an ELM are removed from the database. To study certain pedestal characteristics a cut can be introduced to only include the TS data from the final 25% of the ELM cycle, just before the ELM. At this stage, and for the analysis in section 3, the data is not ELM averaged, due to the low number of ELMs per shot. The data has been ELM averaged at a later stage for the pedestal prediction studies (section 4). The TS pedestal data is then fitted with a modified hyperbolic tangent (mtanh) function [29] to obtain the pedestal parameters (i.e. the pedestal height $X_{e,ped}$, pedestal width ΔX_e, pedestal position $X_{e,pos}$ for the density, temperature and pressure). An example of the TS data and the typical fits to the pedestal profiles are given for n_e and T_e in figure 2.

For MAST plasmas, comparisons of T_i profiles from CXRS and T_e profiles from the TS system were performed in [30, 31]. It was found that $T_i \sim T_e$ in the core, inside the pedestal region. At the pedestal in high collisionality plasmas this is also a good approximation. In low collisionality plasmas at the pedestal top $T_i \sim T_e$ but the gradient of the ion temperature is shallower than the electron temperature so $T_i > T_e$ at the separatrix. Therefore in MAST plasmas, the assumption that $T_i = T_e$ is valid for certain collisionalities and is in general valid at the pedestal top. The total thermal (ion and electron) pressure at the top of the pedestal (p_{ped}) is determined as $p_{ped} = p_{e,ped} + p_{i,ped}$, we use $T_i = T_e$ and the ion density is determined from n_e and Z_{eff}, with carbon as the main impurity.

The database contains a wide range of density and temperature pedestals, the pedestal heights are in the range $n_{e,ped} = 1.2\text{–}6.5 \times 10^{19}$ m^{-3} and $T_{e,ped} = 50\text{–}300$ eV. The pedestal values can be used to calculate the collisionality (ν_e^*), normalised poloidal pedestal pressure ($\beta_{\theta,ped}$), the normalised pressure gradient (α) and the ELM energy loss ($\Delta W/W_{ped}$). The definitions of ν_e^*, $\beta_{\theta,ped}$, α and $\Delta W/W_{ped}$ are given in section 3.1

The SN discharges are dominated by type I ELMs, in comparison to the DN shots, where a variety of ELM types occur. To distinguish the type I and type III ELMs, previous studies on MAST [12] were used. When the ELM frequency is observed as a function of increasing input power a minimum in the ELM frequency for pedestal temperatures of 150 eV was previously found. An associated transition from type III ELMs to type I ELMs occurs at this pedestal temperature. Another high frequency ELM regime, type IV ELMs, occurs on MAST at higher temperatures and lower densities $\left(n_e < 2.0 \times 10^{19}\, m^{-3}\right)$ than the type III ELMs, also known as the low collisionality branch of the type III ELMs. The type IV

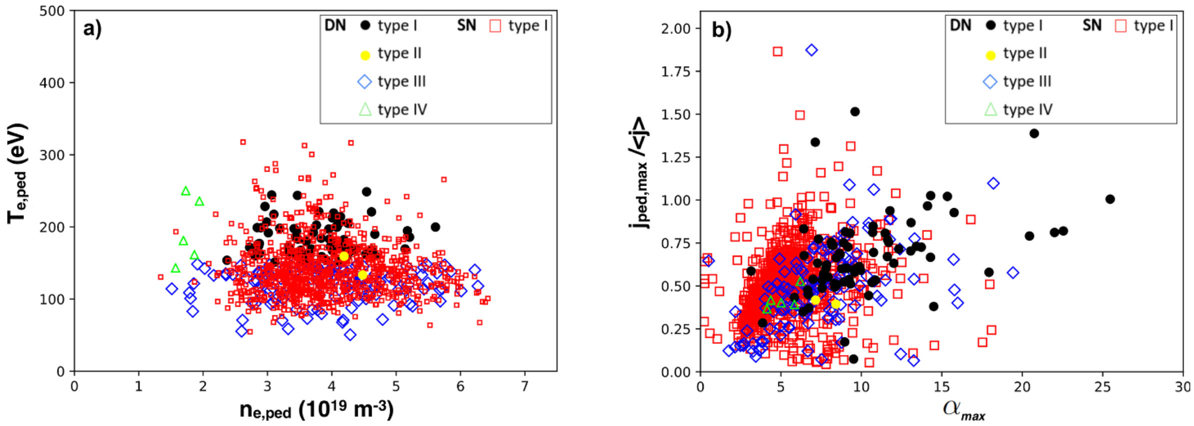

Figure 3. (a) Temperature pedestal height as a function of the density pedestal height. (b) The peak parallel current density as a function of maximum pressure gradient for the different ELM types.

ELMs are obtained on MAST with beam powers over 3 MW and an optimised fuelling scenario [12].

Using a combination of D_α traces and high time resolution fast camera images, we are able to distinguish type II ELMs by their more numerous and uniform filamentary structures compared to other ELM types [14]. Only a limited set of type II ELM data was collected and verified due to the lack of type II ELM shots in the final three campaigns on MAST, and also the limited high time resolution fast camera images, used for verification.

3. Analysing the MAST pedestal database

From the final three MAST campaigns 892 shots with 19 480 TS data time points have been collected. In this section an overview of the database is given, including different ELM types and plasma configurations, comparisons between the inboard and outboard pedestals are performed, and bootstrap current calculations investigated. The type II ELM data is analysed separately in section 5.

3.1. Overview of pedestal data

The pedestal electron temperature ($T_{e,ped}$) and density ($n_{e,ped}$) for all profiles in the last 25% of the ELM cycle are given in figure 3(a). A wide range of pedestal values are seen for the type I ELMs in SN and DN configurations. In general, a higher plasma current was required for the DN shots, therefore, higher temperature pedestals were obtained in comparison to SN. The type III ELMs occur at lower $T_{e,ped}$ over a range of $n_{e,ped}$, whilst the type IV ELMs occur at lower $n_{e,ped}$ over a range of $T_{e,ped}$.

Pedestals that are unstable to type I ELMs are thought to be limited by P-B modes, which are driven by steep pressure gradients and large current density in the edge [32]. Figure 3(b) shows the distribution of the MAST pedestal data, from the final 25% of the ELM cycle, in j-α space. $j_{ped,max}/\langle j\rangle$ is the peak parallel current density in the pedestal region normalised to the averaged plasma current density $\langle j\rangle = I_p/A$, where A is the area of the plasma cross-section. $j_{ped,max}$ is calculated from the addition of the Ohmic current profile from the equilibrium and the contribution from the bootstrap current profile. The bootstrap current has been calculated here from the Sauter formula [15], using the outboard density and temperature profiles. α_{max} is the normalised pressure gradient calculated using the equation in [33]. Figure 3(b) shows the type I ELMs in the DN configuration are located at higher $j_{ped,max}$ and α_{max} associated with the P-B boundary. The SN shots occur over a range of α_{max} and $j_{ped,max}$, as seen in figure 3(b).

The high collisionality type III ELMs are thought to be due to resistive ballooning modes [12, 34], in figure 3(b), they are located at a lower current density but can be found at higher pressure gradients, relative to the other ELMs. The type IV ELMs are located at slightly increased $j_{ped,max}$ and lower pressure gradient in comparison to the type III ELMs. The results are consistent with previous MAST experimental data analysis in [12, 35].

Figure 4 shows various pedestal quantities as a function of the pedestal collisionality (ν_e^*). Here, $\nu_e^* = 6.92 \times 10^{-18}\, R\, q_{95}\, n_{e,ped} \ln\Lambda_e/(T_{e,ped}^2\, \epsilon^{3/2})$, where $\ln\Lambda_e = 31.3 - \ln(\sqrt{n_{e,ped}}/T_{e,ped})$ and ϵ is the inverse aspect ratio. The type I ELMs in the SN configuration cover a large range of collisionalities. The pedestal collisionality does not exceed 2 for the type I ELMs in DN. Type III ELMs are at higher collisionalities, rarely below $\nu_e^* \sim 0.7$, unlike the type IV ELMs that are at a lower collisionality and rarely exceed $\nu_e^* \sim 0.7$. The type II ELM characteristics are discussed in section 5.

The normalised pressure gradient is plotted as a function of the pedestal collisionality in figure 4(a), in general α_{max} decreases with increasing ν_e^* for the type I and III ELMs. The range of α_{max} for the type III ELMs appears to overlap with type I α_{max} values. The type IV ELMs are located at lower α_{max} and ν_e^*. The normalised pedestal poloidal pressure $\beta_{\theta,ped}$ is shown as a function of the collisionality in figure 4(b). The pedestal poloidal beta is calculated using $\beta_{\theta,ped} = 2\mu_0 p_{ped}/B_\theta^2$, as in [36, 37], where the averaged poloidal magnetic field at the pedestal top $B_\theta = \mu_0 I_p/L_p$ and L_p is the circumference of the last closed flux surface. A trend of decreasing $\beta_{\theta,ped}$ with increasing ν_e^* is indicated. Both $\beta_{\theta,ped}$ and ν_e^* depend on $T_{e,ped}$

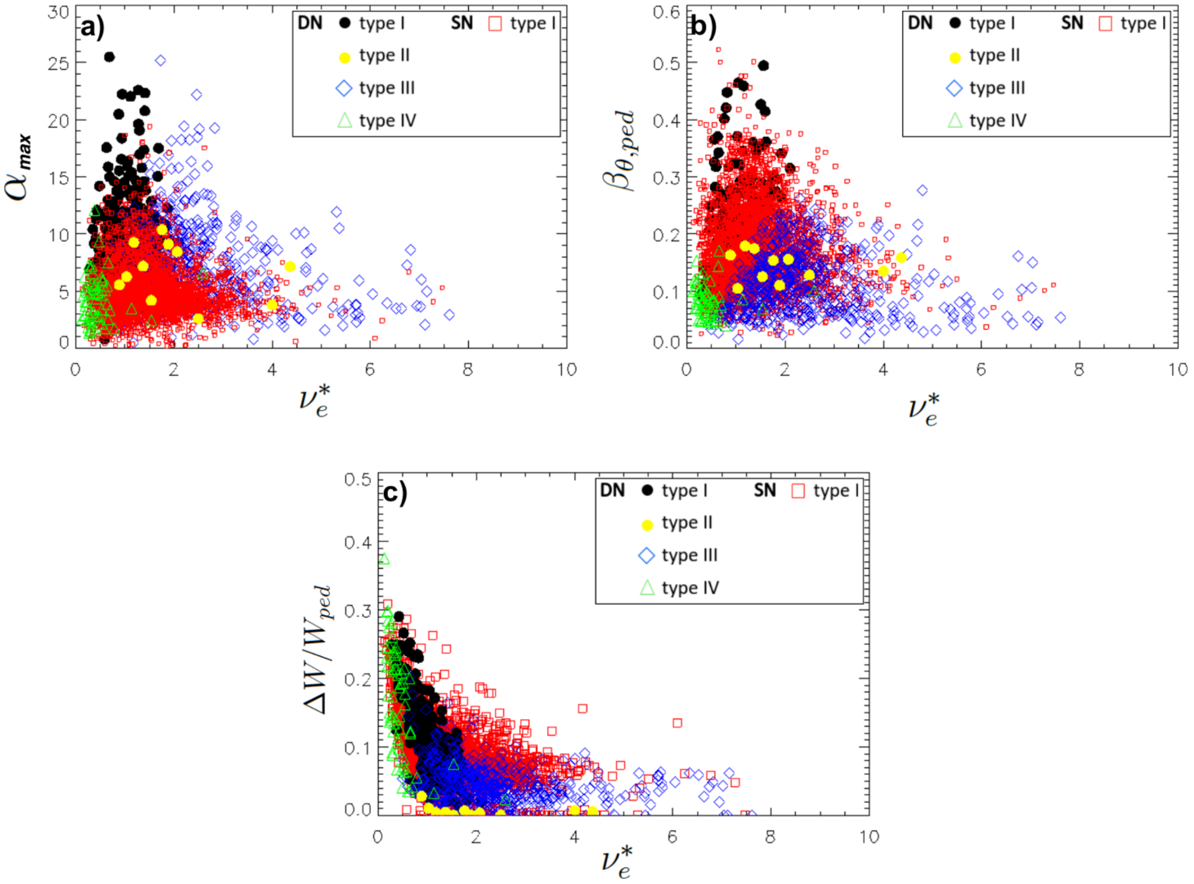

Figure 4. (a) The pressure gradient, (b) the normalised pedestal poloidal pressure and (c) the pedestal energy loss as a function of the collisionality for the different ELM regimes.

and $n_{e,ped}$, with a stronger dependence on $T_{e,ped}$, so the trend shows the dependence of these quantities on $T_{e,ped}$. No trend is observed in figure 3(a) of $T_{e,ped}$ a function of $n_{e,ped}$, therefore it appears that the ν_e^* does not play a very significant independent role in determining the pedestal parameter dependencies, although it sets limits for which type of ELMs occur. The type I ELM regimes reach higher $\beta_{\theta,ped} \leqslant 0.5$ values than the other ELM types. The type III ELMs reach a limit of around $\beta_{\theta,ped} \sim 0.25$ and the type IV ELMs a limit of $\beta_{\theta,ped} \sim 0.15$.

Throughout the ELM cycle, the pedestal energy is higher for type I ELM regimes in DN compared to the SN configuration, where $W_{ped,SN} \sim 0.6 \times W_{ped,DN}$. This is mostly due to the increased plasma volume of the DN, where the volume is ~30% larger in comparison to the SN. The percentage of energy lost from the pedestal ($\Delta W/W_{ped}$) is calculated and shown in figure 4(c), as a function of ν_e^*. $\Delta W/W_{ped}$ is calculated as, $\Delta W/W_{ped} = \Delta n/n_{ped} + \Delta T/T_{ped}$, the first term describes the convective ELM energy losses and the second term the conductive losses. Higher pedestal energy losses are observed for all ELM types with decreasing collisionality. Up to $\Delta W/W_{ped} \sim 30\%$ measured for the type I and IV ELMs, with type III ELMs at lower $\Delta W/W_{ped}$, up to ~12%. On average the type III ELMs have lower $\Delta W/W_{ped}$ than the type I ELMs, but there is an overlap in the pedestal energy losses.

3.2. HFS and LFS pedestal comparison

Determining how the density pedestal structure is formed is important for future tokamaks [38], by comparing the HFS and LFS pedestals the mechanism(s) (neutral fuelling versus transport) could be determined. Future pedestal predictive models could be informed by this, where the pedestal density could be eliminated as an input. At MAST, it is possible to directly compare the HFS and LFS pedestal data from the TS diagnostic. In the MAST database, the SN shots are all fuelled from the LFS, and the DN shots are fuelled from the HFS, either at the mid-plane or at the upper and lower x-points. In [39] the effect on the bootstrap current (j_{BS}) from poloidal asymmetries of the density/fuelling were found to be greater for sources at the HFS. The effect of fuelling position on j_{BS} could play a role in a comparison between SN and DN configurations.

From the database, $T_{e,ped}$ and the pedestal electron temperature width (ΔT_e), in ψ-space, are found to be the same on the HFS and LFS. $n_{e,ped}$ is also the same at the inboard and outboard mid-plane. However, as seen previously on MAST [12] and shown in figure 5(a), the density pedestal width (Δn_e) varies on a flux surface, indicating density is not necessarily a flux surface quantity. Δn_e is in general narrower on the HFS than the LFS, for the DN configuration and to a lesser extent in the

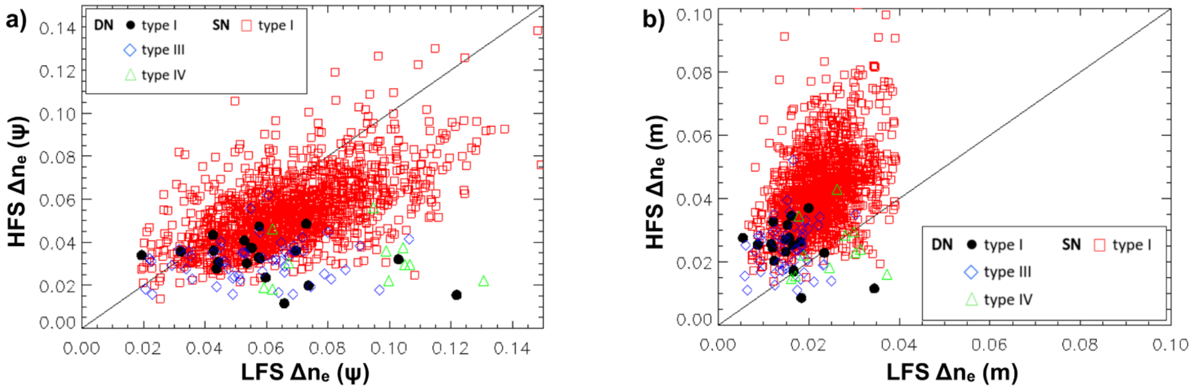

Figure 5. The pedestal density width on the inboard side versus the pedestal density width on the outboard side in (a) ψ-space and (b) in real space.

SN. The type III and IV ELM regimes appear to have an larger discrepancy in Δn_e, and ΔT_e appears to be narrower on the HFS, although more type III and type IV ELM data is needed to confirm this.

Comparing the HFS and LFS pedestals, in real space, it is observed that ΔT_e is wider on the HFS. Δn_e is also wider on the HFS, especially for SN configurations as shown in figure 5(b). It is suggested in [38] that the density pedestal structure is strongly influenced by neutral fuelling but transport effects should not be neglected. The MAST data shows a better correlation for the DN in real space and poor correlation in ψ-space suggesting that here neutral fuelling plays an important role in the pedestal structure. The neutrals do not interact with the magnetic field, so if the pedestal width is determined by neutrals then changes in length scales will depend on plasma parameters in real space and be independent of magnetic geometry and flux surfaces. The opposite is found for the SN configuration, where a stronger correlation is found in ψ-space between the HFS and LFS pedestal widths.

The edge current and pressure pedestal widths are also found to be narrower on the HFS in ψ-space. The narrower inboard pedestal may have an effect on the stability. Currently, MHD codes calculate equilibria assuming flux surface quantities, which as shown here is not always the case. Simulations performed, using JOREK [40–42], are underway to investigate the impact of poloidal variation of density on the MHD stability. Initial studies show the growth rate of the low toroidal mode numbers (peeling modes) were affected, but the growth rate of the high-n (ballooning modes) were unaffected, due to their localisation at the outboard edge, where the pedestal is unchanged. However, further work is required to confirm if this is a physical effect [39], if confirmed a fully predictive pedestal model should account for this, especially when considering equilibria that are unstable to low n modes.

3.3. Bootstrap current calculations and comparisons of analytical formulae

The bootstrap current (j_{BS}) usually dominates the current profile in the edge region. The Sauter formula is widely used for accurately calculating the bootstrap current contribution to the current profile, but has been found to over estimate j_{BS} at high collisionality [43]. Recently, a new analytical formula for calculating the bootstrap current was found [16], here we refer to this as the ‘Redl’ formula for the bootstrap current. The procedure used to determine the bootstrap current coefficients for the Sauter formula was repeated in [16], but derived from the more accurate and reliable numerical code NEO [44, 45], in order to determine the analytical ‘Redl’ formula.

Comparisons of the edge peak bootstrap current, calculated using the Redl and Sauter formulae for the MAST database, are shown in figure 6(a), as a function of ν_e^*. The ratio $j_{BS,Redl}/j_{BS,Sauter}$ decreases with increasing ν_e^*, where there is good agreement around the medium to low range ν_e^*.

The Redl formula has also been implemented in HELENA [17] equilibrium calculations. Several type I ELMy regime shots, in SN and DN configurations, at a range of ν_e^* have been input to HELENA to compare the two models, as seen in figure 6(a), given by the orange stars. From the HELENA calculations, the cases with best and worst agreement of $j_{BS,peak}$ for MAST pedestals with lower $\nu_e^* = 1.0$ and at high $\nu_e^* = 4.2$ respectively are chosen. The edge bootstrap current profiles from these HELENA calculations are shown in figure 6(b). The two calculations agree reasonably well for lower collisionality. At high collisionality the Sauter calculation is significantly increased in the pedestal, as the separatrix region is approached, in comparison to the Redl calculation. A next step, to validate the Redl formula for MAST would be to compare the Redl formula implemented in HELENA with NEO for a range of ν_e^*.

4. MAST ELM data for Europed inputs

In this section we aim to validate the assumptions of Europed using the MAST data. The Europed code is based on the EPED1 model, and is currently being used and developed in an attempt to make consistent pedestal predictions. The experimental data in this section is from the last 25% of the ELM cycle. Only type I ELMs are analysed, in both SN and DN, as currently there is no model within Europed that can be used for predictions of pedestals for other ELM types.

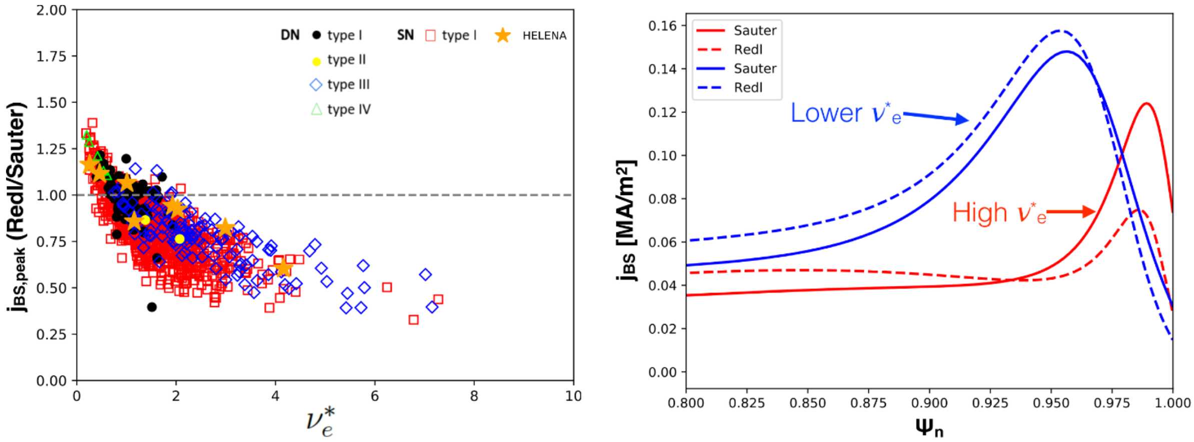

(a) (b)

Figure 6. (a) The ratio of the peak bootstrap current (Redl/Sauter) as a function of collisionality. The stars represent calculations from HELENA. (b) Comparison of edge bootstrap current profiles calculated using the Sauter formula (solid) and the Redl formula (dashed), for MAST pedestals with a lower collisionality $\nu_e^* = 1.0$ (blue) and a high collisionality $\nu_e^* = 4.2$ (red).

Plasma parameters are given as inputs to Europed including global parameters B_T and I_p, the plasma boundary or shaping parameters, $n_{e,ped}$, separatrix density ($n_{e,sep}$), the profile shapes in the core for the density and temperature, as well as the total plasma β and the effective charge Z_{eff}. Most of these parameters can be determined ahead of experiments, but it is much more complex to predict $n_{e,ped}$, $n_{e,sep}$ and Z_{eff}. There is ongoing work, which attempts to eliminate the density pedestal parameters as inputs [18, 39].

When a Europed prediction is performed, a range of pedestal widths are defined, for each pedestal width the equilibrium is solved for in HELENA, before the code tests the ideal MHD stability over a range of toroidal mode numbers ($n = 1, 2, 3, 4, 5, 10, 20, 30, 50, 70$). Here, the ideal MHD code MISHKA [46, 47] is used for the stability calculations. Using the stability results and stability criterion, $\gamma = \gamma_{\text{crit}} = \omega^*/2$ where ω^* is the average diamagnetic frequency defined as half of the maximum diamagnetic frequency in the pedestal region, the code finds the pedestal stability limit, which corresponds to a predicted pedestal profile that is marginally stable.

The model assumes (1) a scaling for the pedestal width, that has been observed on multiple devices [19, 48]. This scaling is heuristically justified on the basis of kinetic ballooning modes (KBMs), providing a constraint on the maximum pedestal width. The relationship between the normalised poloidal pedestal pressure ($\beta_{\theta,ped}$) and the pressure pedestal width (Δp_e) is defined as $\Delta p_e = C\sqrt{\beta_{\theta,ped}}$, where C is the width constant and can be determined from fits to experimental data. (2) The pedestal should be P-B limited. The P-B stability is evaluated, using a range of toroidal mode numbers, in Europed the stability calculation then provides a constraint on the maximum pedestal height. From these assumptions, (1) and (2), a prediction can be made for the pedestal height and width. It is also assumed in Europed that the temperature and density pedestal widths are equivalent ($\Delta T_e = \Delta n_e$) and the ion and electron temperatures are assumed to be the same ($T_i = T_e$).

As previously mentioned, for MAST plasmas, comparisons of T_i profiles from CXRS and T_e profiles from the TS system were performed in [30, 31]. It was found that $T_i = T_e$ is valid for certain collisionalities and is in general valid at the pedestal top, but the T_i and T_e pedestal widths are not equal for low collisionalities.

Originally, in Europed, the density and temperature pedestal widths are assumed equal, and used to determine the pressure pedestal width. This is not necessarily the case for MAST pedestals, as shown in figure 7(a). In the SN configuration $\Delta T_e \sim 0.68 \pm 0.05 \Delta n_e$ and $\Delta T_e \sim 0.81 \pm 0.11 \Delta n_e$ for the DN configuration. Europed now has the functionality to specify this ratio [39]. Using the pedestal width ratio requires more prior knowledge, two more inputs of two known quantities from experiment. A test has been performed with two MAST cases, a SN and a DN case. The width ratio was specified using the values found from the experimental database (given above). Including the width ratio resulted in a less than 3% change in the pedestal height and a less than 2% change in the pedestal width. As this is a minor difference and requires more experimental inputs, the assumption that $\Delta n_e = \Delta T_e$ will be used in the following Europed predictions in this paper.

There is an assumption that the separatrix density is some factor (f) of the pedestal density height $n_{e,sep} = f \times n_{e,ped}$. Figure 7(b) indicates a range of f values. When binned and the weighted mean determined the separatrix density data, calculated at the location where $T_{e,sep} = 40$ eV [49, 50], is reasonably constant across all the MAST shots for the range of pedestal densities. The effect on the pedestal prediction within Europed of the changing separatrix density is minimal on tokamaks such as JET. Previously a scan of f (i.e. $n_{e,sep}$) was performed [18] over a range ($f = 0.1$–0.4). Varying f from 0.1 to 0.6, for a SN and a DN MAST case, resulted in the predicted value of the pedestal temperature height and width changing by less than ∼25% and ∼18% respectively.

The pedestal positions of the density $(n_{e,pos}(\psi))$ and temperature $(T_{e,pos}(\psi))$ are used to analyse the relative shift

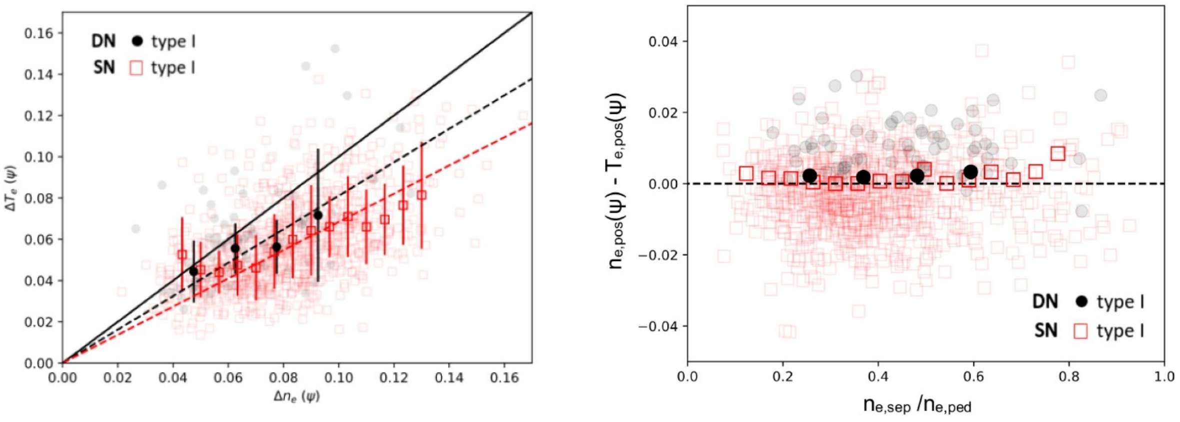

(a)

(b)

Figure 7. The faded data in both (a) and (b) represents the scatter of the data from the database, the data is binned and the weighted mean calculated. The weighted mean is given by the bold data points. (a) The temperature pedestal width versus the density pedestal width in ψ-space, the dashed lines indicate fits to the binned data. (b) The relative shift of the density and temperature pedestal positions ($n_{e,pos}(\psi)$—$T_{e,pos}(\psi)$) versus the ratio of the separatrix density to the pedestal density.

($n_{e,pos}(\psi) - T_{e,pos}(\psi)$) of the profiles. Figure 7(b) indicates the weighted mean data of $n_{e,pos}(\psi)$ is slightly shifted radially outwards from $T_{e,pos}(\psi)$. The relative shift is fairly constant over the range of $n_{e,sep}/n_{e,ped}$ for the MAST data, whereas in JET a correlation is found between these two quantities [51]. In JET ITER-like-wall it has also been shown that this resulting finite relative shift directly impacts Europed predictions of the pedestal [52, 53]. Furthermore, an increased relative shift results in a flattening of the density pedestal radially inward of the separatrix. This leads to a reduction in the normalised density gradient $\nabla n_e/n_e$ and therefore an increase in the parameter $\eta_e \propto (\nabla n_e/n_e)^{-1}$. This in turn can lead to more virulent electron temperature gradient microinstabilities and therefore increased levels of turbulent heat transport [51, 54, 55]. The role of the relative shift on both turbulent heat transport and Europed predictions in MAST is therefore something that should be verified in future work.

If experimental data is available, it is possible to verify if a particular case is close to the P-B stability boundary, giving an indication of whether the Europed prediction will be reasonable, where the pedestal should be limited by P-B modes. ESSIVE is used to check the stability, it uses HELENA to generate equilibria within a range of j and α space. MISHKA is then used to test the MHD stability of each equilibrium, over a range of toroidal mode numbers ($n = 1, 2, 3, 4, 5, 10, 20, 30, 50, 70$). P-B diagrams are shown in figures 8(a) and (b) for examples of a MAST DN and SN configuration respectively. These shots were chosen as they cover a large range of MAST global and shaping parameter space (parameters given in figure 8). The shots also have long periods of type I ELMs with a high amount (for MAST) of ELM cycles, such that ELM averaged profiles can be used. In both configurations the experimental point is located in the unstable region close to the ballooning boundary, consistent with [21]. Note that not all MAST type I ELMs are in this unstable region.

The MAST data is used to determine if the KBM constraint on the pedestal width, $\Delta p_e = C\sqrt{\beta_{\theta,ped}}$, is a good approximation for MAST. Δp_e is shown as a function of $\beta_{\theta,ped}$, in figure 9 for the type I ELM regimes in the SN and DN configurations. In Europed $\Delta p_e = (\Delta n_e + \Delta T_e)/2.0$ is used. As shown by comparing figure 9(a) with figure 9(b) the two are not equivalent in MAST. From the pedestal database it is found that $\Delta p_e \sim 0.8 \times (\Delta n_e + \Delta T_e)/2.0$, therefore, the pressure width for MAST could be incorrectly predicted by Europed. The faded data points in figure 9 represent the scatter of data from the database. This data is then binned and the weighted mean calculated, shown by the bold data points with error bars. Each of the bins requires at least ten data points for statistical purposes, and the error bars represent the standard error of the mean. In figure 9 the solid lines indicate the linear fit to $\sqrt{\beta_{\theta,ped}}$ for the weighted mean data, where a value for C is given in the figure. The dashed lines show the fit to the weighted mean data, where $\Delta = C(\beta_{\theta,ped})^b$, both C and the exponent b decrease in this fit. The values of C and b are also given in figure 9. The value of b is consistent with 0.5 within the errors, and the fit to $\sqrt{\beta_{\theta,ped}}$ is reasonable for the weighted mean data, so the constraint could be valid for the MAST pedestal predictions, with the correct choice of C. However, the scatter of the pedestal width spans a factor $\gtrsim 2$. Thus, we cannot conclude that $\beta_{\theta,ped}$ is the only parameter that affects the pedestal width.

A test is performed in Europed where C is scanned, the predicted pedestal height and width can then be compared to the experimental values. This was done for MAST shots #29782 (SN) and #30422 (DN). The averaged profiles from the last 25% of the ELM cycle are used from the type I ELMy period. Figure 10 shows the results of the width constant scan. As C is increased both the pedestal height and width increase. The dashed line indicates agreement between the Europed prediction and the experimental value. The prediction agrees with the experimental values at different C for the pedestal height and

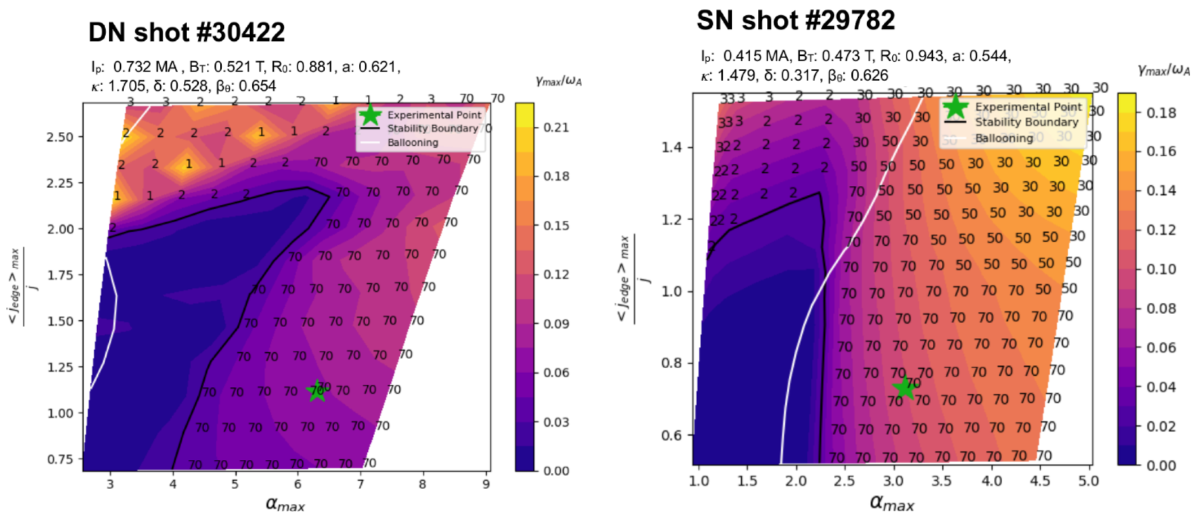

(a) (b)

Figure 8. The stability plots for (a) a DN (shot #30422) and (b) a SN (shot #29782) discharge. The green star represents the experimental point, the solid black line indicates the stability boundary with the criterion $\gamma = 0.03\omega_A$ and the white line shows the infinite n ballooning boundary. $\langle j_{edge}\rangle$ is the flux surface averaged toroidal current density.

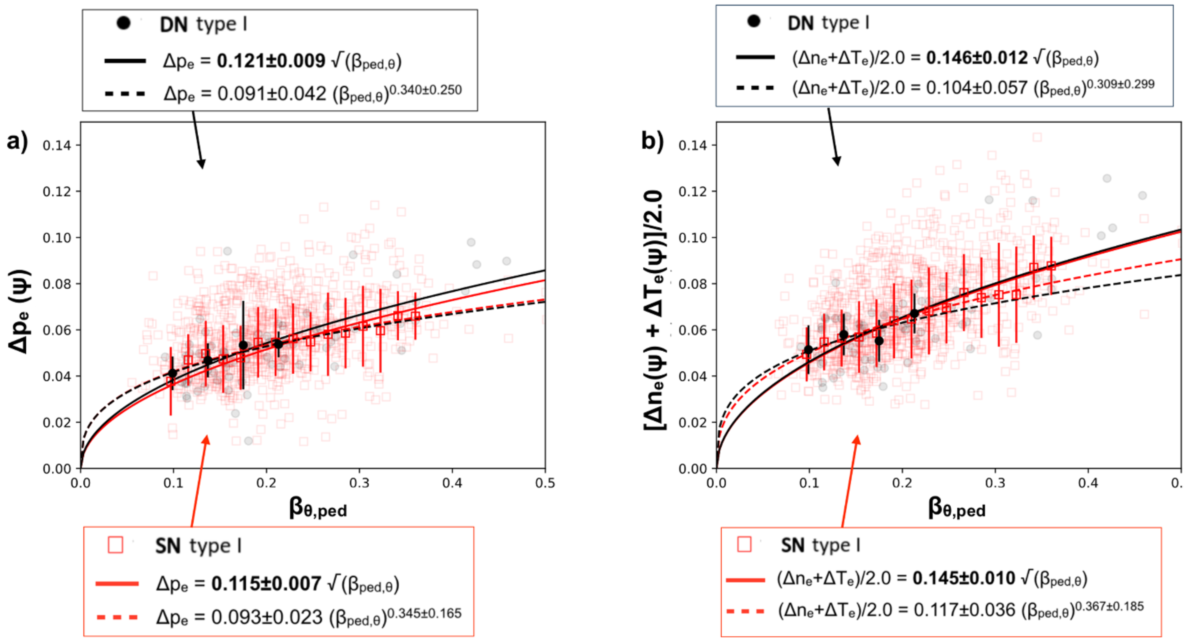

Figure 9. (a) The pressure pedestal width as a function of the pedestal normalised poloidal pressure. (b) The pressure width averaged from the density and temperature pedestal widths as a function of $\beta_{\theta,ped}$.

width. The temperature pedestal height is correctly predicted at $C \sim 0.13$ for the DN case and $C \sim 0.145$, for the SN. This is also the case for the pedestal pressure.

The temperature pedestal height is predicted to within 10% for the value of C calculated from the $\sqrt{\beta_{\theta,ped}}$ fit to the experimental data, when $\Delta p_{e,av}$ is used (figure 9(b)), for both cases. However, the pedestal width is overestimated for the same value of C, the correct pedestal width is predicted at a lower value of $C \sim 0.10$–0.11. The DN pedestal height and width are predicted at lower values of the width constant in comparison to the SN configuration.

The discrepancy in the pedestal width, whilst the pedestal height is correctly predicted, could be attributed to several reasons considered here. An accurate measurement of the pedestal width from experiment is difficult and these values have large errors. Therefore, we could be comparing to an inaccurate experimental pedestal width. The shots investigated here, whilst in the unstable region, are rather far from the P-B stability boundary and so the width and height are not simultaneously predicted correctly using the P-B limited case from Europed. This discrepancy has also been observed in JET studies [56]. If the experimental pedestals were located on the P-B

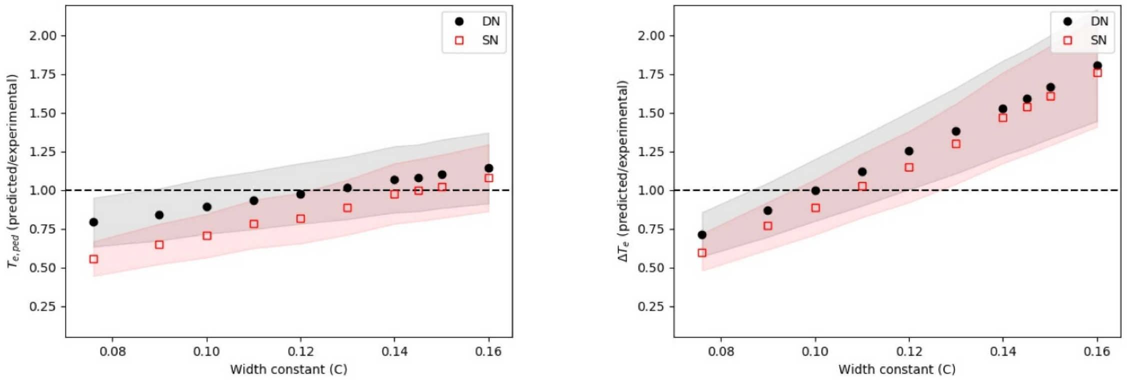

(a) (b)

Figure 10. A scan in C for a SN and a DN case showing (a) the pedestal temperature height and (b) the pedestal temperature width. The predicted values are normalised to the experimental value, where the dashed black line indicates agreement. The shaded area indicates $\pm 20\%$ of the normalised values.

stability boundary, on the stability plots, then it is expected that the correct height and width would be predicted by Europed. In spherical tokamaks the sheared rotation can also effect P-B stability [57] and could be a further reason for the discrepancy.

The choice of the width constant is important as this can have a significant effect on the pedestal prediction, this should be kept in mind when attempting to make reliable pedestal predictions for spherical tokamaks, such as MAST-U and beyond toward tokamaks such as STEP.

5. Type II ELM regimes and stability analysis

A potential H-mode regime for future spherical tokamaks could be a type II ELM regime and research is underway to investigate this. Type II ELMs are small, releasing less pedestal energy during an event and thus lower heat fluxes reach divertor targets. Here, type II ELMs from the MAST pedestal database are analysed. Ideal MHD stability analysis and parameter scans are performed using ESSIVE, where comparisons between type I and type II ELMs are made.

Type II ELM regimes in MAST [14] have only been observed in DN, where the plasma is highly shaped. Comparisons have previously been made for type II ELMs in MAST plasmas to other tokamaks, such as NSTX [25] and ASDEX Upgrade [14], where similar characteristics have been identified on each device. In MAST, one difference to the ASDEX Upgrade type II regime, is the type II ELM filaments have low density, this results in low density transport. The pedestal can then evolve and trigger a type I ELM. MAST type II ELM regimes are interspersed with type I ELMs, whereas at ASDEX Upgrade [14], the higher density pump out can allow for a sustained type II ELM regime. It has been suggested that the type II ELMs at ASDEX Upgrade might be ballooning modes, which are localised close to the separatrix [23]. Here, stability analysis is performed for type II ELMs on MAST.

5.1. Analysis of type II experimental data

In general the type II ELM filaments are thought to originate closer to the LCFS, with lower toroidal and radial velocities, and do not appear to detach. The type II ELMs have the highest toroidal mode number (n) compared to other ELM types, where $n \sim 20$–30, indicating more of a ballooning mode [14]. In figure 11 fast camera images are shown for a type I and a type II ELM, where the ELMs are indicted on the D_α trace. The type II ELMs appear as small peaks on the D_α trace (a zoom of the D_α trace from figure 1(g)), the larger peaks indicate type I ELMs. The fast camera shows uniform and numerous filaments for the type II ELMs, whereas non-linear and fewer larger filaments are observed during the type I ELMs.

Type II ELMs occur at higher collisionality in MAST, $\nu_e^* \geqslant 1$, as shown in figures 4(a)–(c). This limit is consistent with previous observations in [25]. Figure 4(b) shows an upper limit of ~ 0.2 for $\beta_{\theta,ped}$ for the type II ELMs, a limit of $\beta_{ped} \sim 0.05$ is also found. Again, the results are consistent with previous findings [14, 25], and at larger pedestal β type I ELMs occur.

Pedestal energy losses are consistently lower for the type II ELMs, compared to the other ELM types, where $\Delta W/W_{ped} < 3\%$, as shown in figure 4(c). During the type II ELM crash $T_{e,ped}$ remains constant so only the convective part of ΔW is calculated here.

The type II ELM regimes can cover a range of pedestal heights, where $T_{e,ped}$ is mostly between the type I and type III ELMs in DN. $n_{e,ped}$ in a type II regime is similar to that for the type I. Figure 3 shows only two data points for the type II ELMs in the final 25% of the ELM cycle, due to lack of data it is difficult to draw conclusions but it appears that the type II ELMs (yellow circles figure 3(b)) are positioned at lower $j_{ped,max}$ and α_{max} relative to the type I ELMs in DN configuration (black circles).

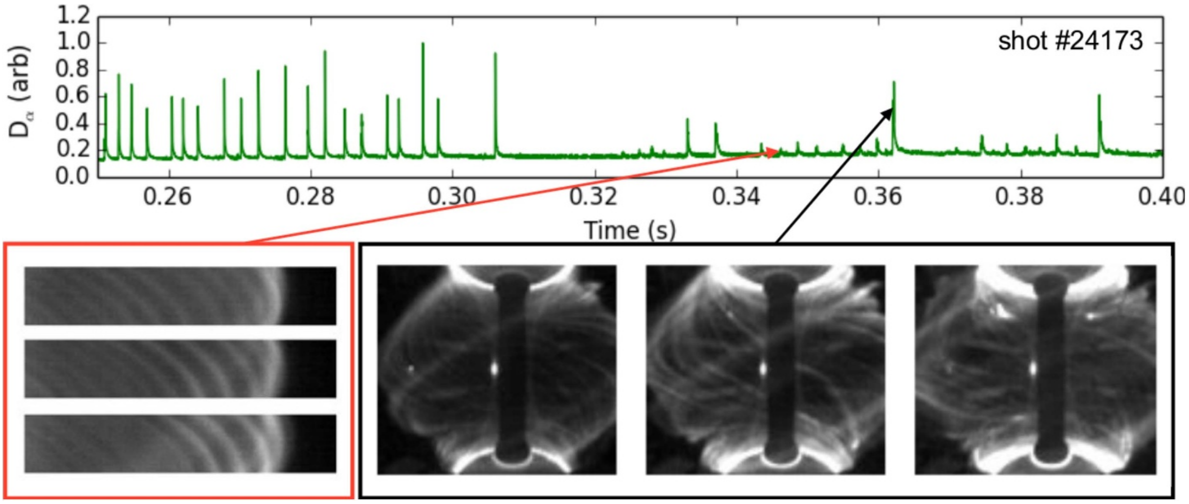

Figure 11. The D_α trace for shot #24173 given above with fast camera frames, focused at the plasma edge, during the small ELM at $t = 346$ ms (within the red outline on the left), and images during the type I ELM at $t = 363$ ms (within the black outline).

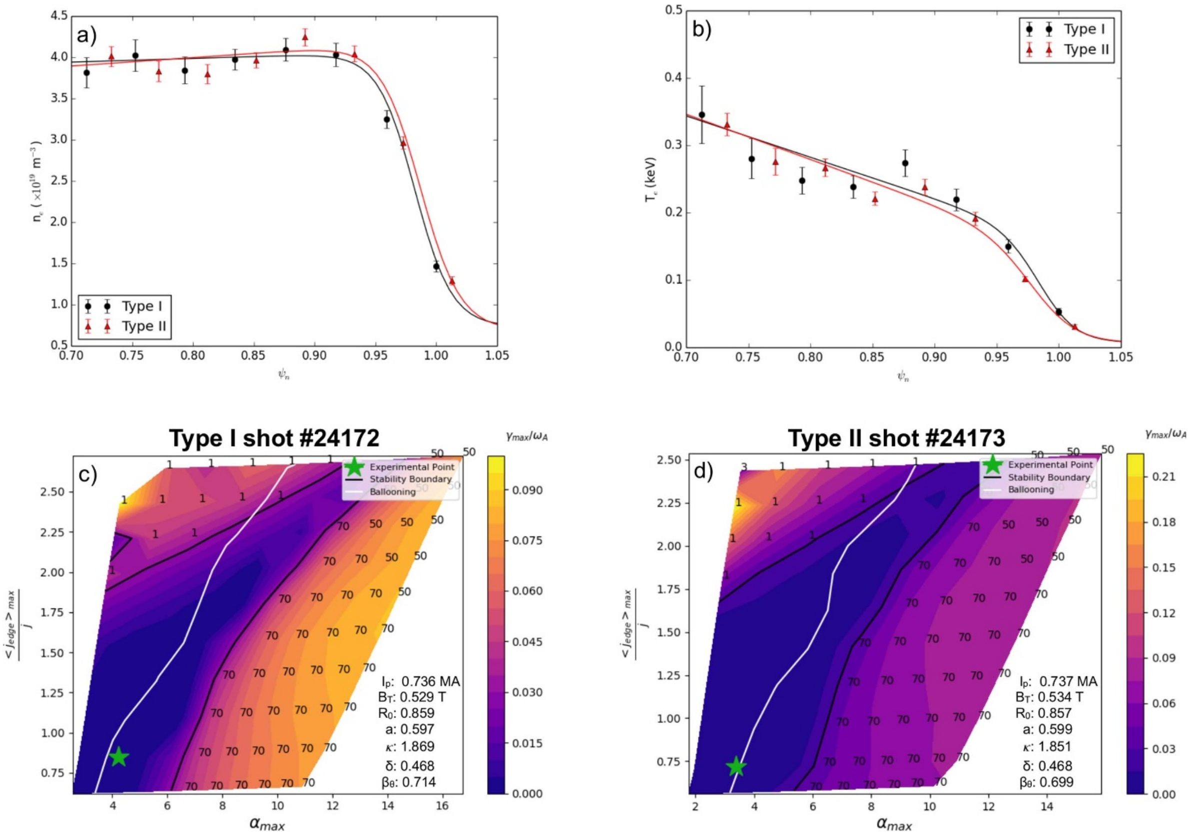

Figure 12. (a) Density and (b) temperature profiles prior to a type I and type II ELM. Stability plots for (c) type I and (d) type II ELMs, produced using ESSIVE. The green star represents the experimental point, the solid black line indicates the stability boundary with the criterion $\gamma = 0.03\omega_A$ and the white line shows the infinite n ballooning boundary. $\langle j_{edge}\rangle$ is the flux surface averaged toroidal current density.

5.2. Ideal MHD stability analysis of type II ELMs

Ideal MHD stability analysis of the type II ELMs indicates whether the pedestal is located close to the P-B boundary. The profiles just before a type I ELM from shot #24172 and a type II ELM from shot #24173 are input into ESSIVE to investigate P-B stability. Shot #24173 is a repeat of #24172, these shots have very similar global and shaping parameters, and are given in figure 12. The D_α traces for each shot show type II ELM regimes interspersed with type I ELMs.

The electron temperature and density profiles are for a single TS time point taken from the last 25% of the ELM cycle,

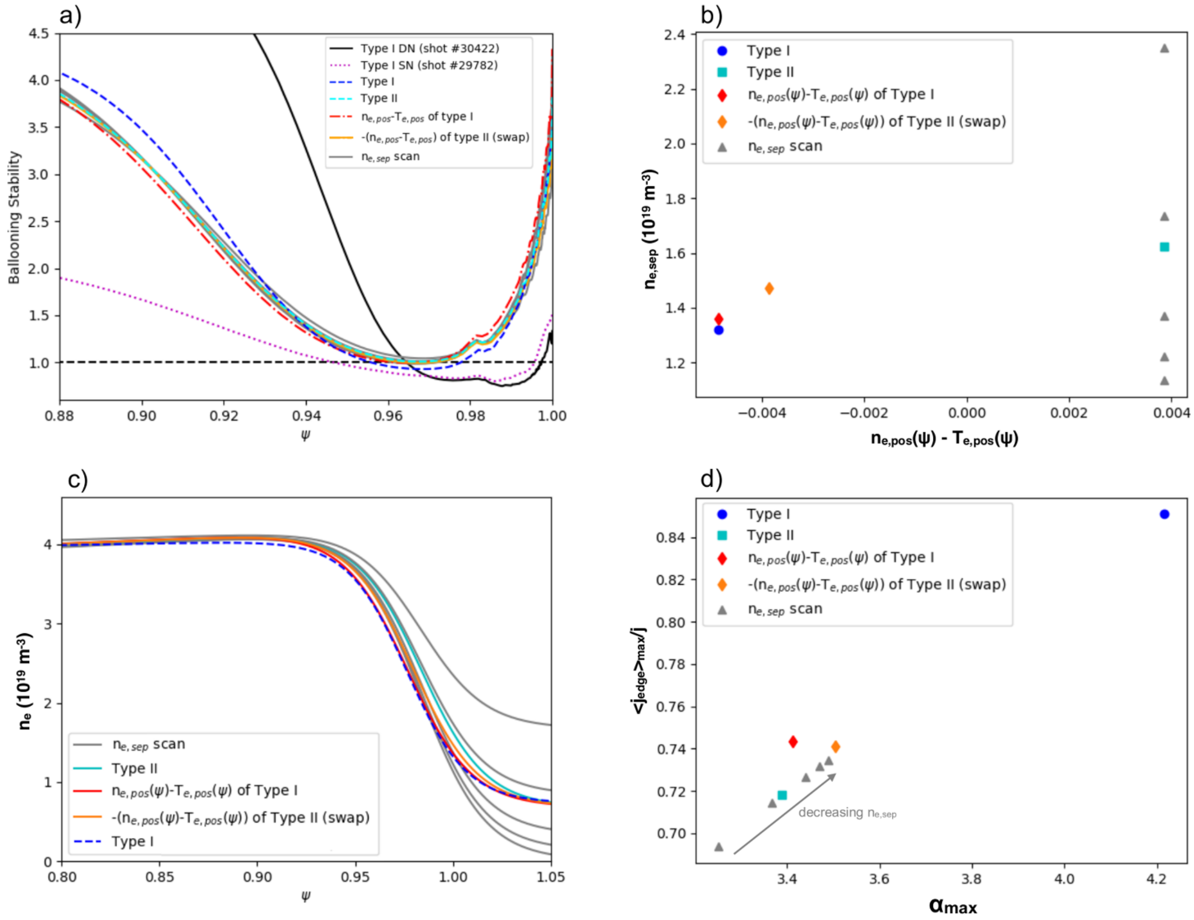

Figure 13. (a) The ballooning stability profiles for the parameter scans. The horizontal black dashed line represents the ballooning stability threshold (below 1 is ballooning unstable). (b) Values of the relative shift $(n_{e,pos}(\psi) - T_{e,pos}(\psi))$ and $n_{e,sep}$ for the type I and type II cases along with scans in the separatrix density and the relative pedestal position, where the density profiles for each of the cases are provided in (c). (d) The $j - \alpha$ values for the type I and II profiles and the scans in $n_{e,pos}(\psi) - T_{e,pos}(\psi)$ and $n_{e,sep}$.

shown in figures 12(a) and (b). It was not possible to use time averaged profiles for the analysis due to lack of data at the end of the ELM cycles, in the type II ELM shots. The type I and type II profiles are similar, with very little difference between the pedestal profiles. Again, ESSIVE is used to investigate the ideal MHD stability, over a range of toroidal mode numbers ($n = 1, 2, 3, 4, 5, 10, 20, 30, 50, 70$).

The stability plots for the type I and II ELMs are shown in figures 12(c) and (d) respectively. As expected due to the similarities in the input profiles the stability diagrams are alike. The type II ELM experimental point is located at a lower $\langle j_{edge}\rangle_{max}$ and α_{max}, compared the type I ELM. Both the type I and II pedestals are in the stable region of the P-B stability diagram, but the type I ELM is locally marginally unstable to $n = \infty$ ballooning modes at around $\psi_n = 0.963$–0.975, as shown in figure 13(a), comparing the type II (cyan dashed line) and the type I (blue dashed line) ELMs. There is not much to distinguish the type I and the type II ELM cases shown here. The same result, in relation to ideal MHD stability, has been found for the only other type II ELM, from this MAST database, for which there was TS data in the last 25% of the ELM cycle.

The stable region is extended at the P-B nose in the stability plot. A test has been performed, in this region, with increased poloidal resolution and also using ELITE for the stability analysis, in each case this region remained stable.

In most MAST type I regimes, that are not mixed with type II ELMs, the experimental point is positioned on or close to the ballooning boundary [21]. As shown in section 4, the type I pedestal experimental point is usually at a lower current density than the P-B nose and is usually ballooning unstable. From figure 13(a) it is shown that, the pure type I ELM regimes, from section 4 in the SN (dotted magenta line) and DN (black solid line) configurations, are marginally unstable to $n = \infty$ ballooning modes across the pedestal. Especially, in comparison to the mixed type I and type II regimes, which are close to the stability boundary. In the future it would be interesting to investigate if this is the case for other spherical tokamaks by exploring type II ELMs in MAST-U and NSTX. The pure type I ELM DN shot #30422 has similar global and shaping parameters as the type II shots, the most significant difference is the input power. The input power for the pure type I ELM regime is over double that of the type I/II mixed regimes, this is consistent with the power scan given in [14], as the input power was increased the type II ELMs disappeared and type I ELM regime was established. The fits to the TS profile data, which are input to ESSIVE, indicate the T_e, n_e and p_e

pedestal gradients are increased in shot #30422, in comparison to the type I and II profiles from the mixed regimes, resulting in the differences observed in the stability plots.

5.3. Effect of $n_{e,sep}$ and pedestal relative shift on stability

At ASDEX Upgrade, a higher separatrix density is observed during the type II ELM regime [14, 23]. A scan in the separatrix density is performed here, starting from the type II ELM case, to determine the effect on stability. Figure 13(b) indicates the range of separatrix densities (grey triangles), which are used in the scan. The density profiles are shown in figure 13(c). A wide range of separatrix densities have been scanned whilst the pedestal height remains fairly constant and the temperature profile remains unchanged. The values of $\langle j_{edge}\rangle_{max}$ and α_{max} are given in figure 13(d). Note that the axes in figure 13(d) are different to the $j-\alpha$ plots in figure 12 and only small changes in the pressure gradient and current density occur. As $n_{e,sep}$ is decreased $\langle j_{edge}\rangle_{max}$ and α_{max} increase. However, even at separatrix densities lower than the type I ELM case the higher type I values of $\langle j_{edge}\rangle_{max}$ and α_{max} are not reached. $n_{e,ped}$ was decreased from the type II to the type I value, this resulted in a decrease in $\langle j_{edge}\rangle_{max}$ and α_{max}.

From the experimental profiles in figures 12(a) and (b) the relative shift ($n_{e,pos}(\psi)-T_{e,pos}(\psi)$) of the pedestal positions appears to be one of the differences between the type I and type II profiles. $n_{e,pos}(\psi)-T_{e,pos}(\psi)$ was varied, as shown in figure 13(b), and the density profiles are given in figure 13(c). First, the negative value of $n_{e,pos}(\psi)-T_{e,pos}(\psi)$ of the type II ELM is used to create new profiles for stability analysis. The orange diamonds in figures 13(b) and (d) represent this case. Using ESSIVE, the stability analysis indicates an increase in $\langle j_{edge}\rangle_{max}$ and α_{max}, when $n_{e,pos}(\psi)-T_{e,pos}(\psi)$ is decreased.

Then, $n_{e,pos}(\psi)-T_{e,pos}(\psi)$ is switched from the positive type II (cyan square) to the negative type I value (red diamond), note changing the relative shift also alters the separatrix density slightly. Using the new value for $n_{e,pos}(\psi)-T_{e,pos}(\psi)$ the density profile is very similar to that of the type I ELM profile in figure 12(a), but the temperature pedestal has a lower gradient, which results in a lower maximum pressure gradient. From the stability analysis, the decrease in $n_{e,pos}(\psi)-T_{e,pos}(\psi)$ again results in an increase in $\langle j_{edge}\rangle_{max}$ and α_{max}, comparing red diamond and cyan square in figure 13(d).

The ballooning stability calculation performed in HELENA indicates only small differences are observed in the pedestal region from the scans, as shown in figure 13(a). For the negative relative shift and the three lowest separatrix density cases the pedestal is only just locally ballooning unstable, at around $0.963 < \psi < 0.973$. As the separatrix density is decreased the pedestal region becomes more ballooning unstable. No single pedestal parameter, which has been explored here, with the ideal MHD code, is alone responsible for the difference between the type I and type II ELMs. To confirm these results, they should be repeated for more type II ELMs; here we have focused on one specific profile.

6. Summary and outlook

The MAST pedestal data obtained using the upgraded TS system for the final three campaigns on MAST, is presented, allowing for an overview of pedestal characteristics. Trends in the different ELM types have been discussed and pedestal characteristics are consistent with previous MAST pedestal results in [12]. Direct comparisons of the HFS and LFS pedestal data were performed. The SN shots are all fuelled from the LFS and DN shots from HFS, where the effect of fuelling position on bootstrap current could play a role in the comparison. The density appears to vary on a flux surface, where the pedestal width is, in general, narrower on the HFS. This should be considered when performing density pedestal predictions, especially if the MHD stability is affected. Bootstrap current calculations for the MAST database have been obtained and comparisons of the Sauter and Redl formulae are performed. The two calculations agree at low ν_e^*, but deviate at higher ν_e^*.

The assumptions for Europed have been tested with MAST data in anticipation of future spherical tokamak pedestal predictions. Most Europed assumptions hold including the KBM constraint on the pedestal width, where the value of the width constant was evaluated from the MAST database. It was found that $C\sim 0.145$ for MAST, this is almost twice that of previous studies on conventional tokamaks, where $C = 0.076$ was obtained [19]. Using the attained value, $C\sim 0.145$, first MAST pedestal predictions were performed. The temperature pedestal height was predicted to within 10% for a SN and a DN shot. The pedestal height can be closely predicted using the width constant determined by experimental data, but the pedestal width is overestimated for the same value of C. This discrepancy could be due to inaccurate pedestal width measurements, the distance of the experimental point from the P-B stability boundary, or the rotational shear effect on P-B stability in spherical tokamaks. The MAST pedestal predictions using $C = 0.145$ will be further confirmed with more cases in future work using Europed for the pedestal analysis.

Analysis of the MAST type II ELMs is performed. The stability analysis is performed with ESSIVE and indicates that both the type I and II ELMs in the mixed regimes have similar MHD stability properties, and are therefore difficult to distinguish using ideal MHD alone. Both are P-B stable unlike the type I ELM from a purely type I regime, which is located in the ballooning region of the stability diagram. Parameter scans of decreasing $n_{e,sep}$ and $n_{e,pos}(\psi)-T_{e,pos}(\psi)$ resulted in an increase in the maximum edge current density and pedestal pressure gradient. No threshold to a type I ELM was observed when individually varying these parameters.

The MAST pedestal data has been analysed here. The data has been used to validate the Europed assumptions, where more confidence can be given to the Europed pedestal predictions. Future work could include confirming the results from the experimental database with data from other spherical tokamaks, such as NSTX and MAST-U, to determine if the ELM features, which are observed here, are consistent. In particular NSTX and MAST-U experiments with low collisionality plasmas for reactor relevant studies. This could allow stronger conclusions to be drawn and the knowledge could contribute to future spherical tokamaks.

Data availability statement

The data that support the findings of this study are available upon reasonable request from the authors.

Acknowledgments

This work has been carried out within the framework of the EUROfusion Consortium and has received funding from the Euratom research and training programme 2014–2018 and 2019–2020 under Grant Agreement No. 633053 and from the RCUK [Grant Number EP/T012250/1]. To obtain further information on the data and models underlying this paper please contact PublicationsManager@ukaea.uk. The views and opinions expressed herein do not necessarily reflect those of the European Commission.

ORCID iDs

S F Smith https://orcid.org/0000-0003-2319-0356
A Kirk https://orcid.org/0000-0002-5746-6595
B Chapman-Oplopoiou https://orcid.org/0000-0001-9879-2285
J G Clark https://orcid.org/0000-0002-1578-2346
C J Ham https://orcid.org/0000-0001-9190-8310
L Horvath https://orcid.org/0000-0002-5692-6772
C F Maggi https://orcid.org/0000-0001-7208-2613
S Saarelma https://orcid.org/0000-0002-6838-2194

References

[1] Wagner F *et al* 1982 Regime of improved confinement and high beta in neutral-beam-heated divertor discharges of the ASDEX tokamak *Phys. Rev. Lett.* **49** 1408–12
[2] Kirk A *et al* 2006 Evolution of filament structures during edge-localized modes in the MAST tokamak *Phys. Rev. Lett.* **96** 185001
[3] Zohm H 1996 Edge localized modes (ELMs) *Plasma Phys. Control. Fusion* **38** 105–28
[4] Eich T, Sieglin B, Thornton A J, Faitsch M, Kirk A, Herrmann A and Suttrop W 2017 ELM divertor peak energy fluence scaling to ITER with data from JET, MAST and ASDEX upgrade *Nucl. Mater. Energy* **12** 84–90
[5] Viezzer E 2018 Access and sustainment of naturally ELM-free and small-ELM regimes *Nucl. Fusion* **58** 115002
[6] Fishpool G, Canik J, Cunningham G, Harrison J, Katramados I, Kirk A, Kovari M, Meyer H and Scannell R 2013 MAST-upgrade divertor facility and assessing performance of long-legged divertors *J. Nucl. Mater.* **438** S356–9
[7] Scannell R, Walsh M J, Dunstan M R, Figueiredo J, Naylor G, O'Gorman T, Shibaev S, Gibson K J and Wilson H 2010 A 130 point Nd:YAG Thomson scattering diagnostic on MAST *Rev. Sci. Instrum.* **81** 10D520
[8] Scannell R *et al* 2008 Design of a new Nd:YAG Thomson scattering system for MAST *Rev. Sci. Instrum.* **79** 10E730
[9] Wilson H, Chapman I, Denton T, Morris W, Patel B, Voss G and Waldon C (The STEP Team) 2020 STEP—on the pathway to fusion commercialization *Commercialising Fusion Energy* (Bristol: IOP Publishing)
[10] Kirk A *et al* (The MAST Team) 2004 ELM characteristics in MAST *Plasma Phys. Control. Fusion* **46** 551–72
[11] Kirk A, Counsell G F, Arends E, Meyer H, Taylor D, Valovic M, Walsh M and Wilson H (The MAST Team) 2004 H-mode pedestal characteristics on MAST *Plasma Phys. Control. Fusion* **46** A187–94
[12] Kirk A, O'Gorman T, Saarelma S, Scannell R and Wilson H R 2009 A comparison of H-mode pedestal characteristics in MAST as a function of magnetic configuration and ELM type *Plasma Phys. Control. Fusion* **51** 065016
[13] Kirk A *et al* (MAST and ASDEX Upgrade Teams) 2015 Effect of resonant magnetic perturbations on low collisionality discharges in MAST and a comparison with ASDEX Upgrade *Nucl. Fusion* **55** 043011
[14] Kirk A, Muller H W, Wolfrum E, Meyer H, Herrmann A, Lunt T, Rohde V and Tamain P 2011 Comparison of small edge-localized modes on MAST and ASDEX Upgrade *Plasma Phys. Control. Fusion* **53** 095008
[15] Sauter O, Angioni C and Lin-Liu Y R 1999 Neoclassical conductivity and bootstrap current formulas for general axisymmetric equilibria and arbitrary collisionality regime *Phys. Plasmas* **6** 2834–9
[16] Redl A, Angioni C, Belli E and Sauter O 2021 A new set of analytical formulae for the computation of the bootstrap current and the neoclassical conductivity in tokamaks *Phys. Plasmas* **28** 022502
[17] Huysmans G T A, Goedbloed J P and Kerner W 1991 Isoparametric bicubic hermite elements for solution of the Grad–Shafranov equation *Int. J. Mod. Phys.* C **02** 371–6
[18] Saarelma S, Challis C D, Garzotti L, Frassinetti L, Maggi C F, Romanelli M and Stokes C 2018 Integrated modelling of H-mode pedestal and confinement in JET-ILW *Plasma Phys. Control. Fusion* **60** 014042
[19] Snyder P B, Groebner R J, Leonard A W, Osborne T H and Wilson H R 2009 Development and validation of a predictive model for the pedestal height *Phys. Plasmas* **16** 056118
[20] Snyder P B, Groebner R J, Hughes J W, Osborne T H, Beurskens M, Leonard A W, Wilson H R and Xu X Q 2011 A first-principles predictive model of the pedestal height and width: development, testing and ITER optimization with the EPED model *Nucl. Fusion* **51** 103016
[21] Knolker M, Osborne T, Belli E, Henderson S, Kirk A, Kogan L, Saarelma S and Snyder P B 2021 Pedestal stability analysis on MAST in preparation for MAST-U *Nucl. Fusion* **61** 046041
[22] Saibene G *et al* 2002 Improved performance of ELMy H-modes at high density by plasma shaping in JET *Plasma Phys. Control. Fusion* **44** 1769–99
[23] Harrer G F *et al* 2018 Parameter dependences of small edge localized modes (ELMs) *Nucl. Fusion* **58** 112001
[24] Stober J, Maraschek M, Conway G D, Gruber O, Herrmann A, Sips A C C, Treutterer W and Zohm H (ASDEX Upgrade Team) 2001 Type II ELMy H modes on ASDEX Upgrade with good confinement at high density *Nucl. Fusion* **41** 1123–34
[25] Maingi R, Hubbard A E, Meyer H, Hughes J W, Kirk A, Maqueda R and Terry J L 2011 Comparison of small ELM characteristics and regimes in Alcator C-Mod, MAST and NSTX *Nucl. Fusion* **51** 063036
[26] Scannell R, Walsh M J, Carolan P G, Conway N J, Darke A C, Dunstan M R, Hare D and Prunty S L 2006 Enhanced edge Thomson scattering on MAST *Rev. Sci. Instrum.* **77** 10E510
[27] Walsh M J, Conway N J, Dunstan M, Forrest M J and Huxford R B 1999 Interactive optical design and realization of an optimized charge coupled device Thomson scattering

system for the spherical tokamak START *Rev. Sci. Instrum.* **70** 742–6
[28] ARENDS E R 2003 Density gradients in spherical tokamak plasmas *PhD Thesis* Technische Universiteit Eindhoven
[29] Scannell R, Beurskens M, Carolan P G, Kirk A, Walsh M, O'Gorman T and Osborne T H 2011 Deconvolution of Thomson scattering temperature profiles *Rev. Sci. Instrum.* **82** 053501
[30] Morgan T 2011 Measurement of MAST edge ion temperatures and velocities *PhD Thesis* University of York
[31] Lloyd B *et al* 2011 Overview of physics results from MAST *Nucl. Fusion* **51** 094013
[32] Wilson H R, Connor J W, Field A R, Fielding S J, Miller R L, Lao L L, Ferron J R and Turnbull A D 1999 Ideal magnetohydrodynamic stability of the tokamak high-confinement-mode edge region *Phys. Plasmas* **6** 1925
[33] Miller R L, Chu M S, Greene J M, Lin-Liu Y R and Waltz R E 1998 Noncircular, finite aspect ratio, local equilibrium model *Phys. Plasmas* **5** 973–8
[34] Sartori R *et al* 2004 Study of type III ELMs in JET *Plasma Phys. Control. Fusion* **46** 723–50
[35] Meyer H *et al* 2009 Overview of physics results from MAST *Nucl. Fusion* **49** 104017
[36] Diallo A *et al* 2011 Dynamical evolution of pedestal parameters in ELMy H-mode in the National Spherical Torus Experiment *Nucl. Fusion* **51** 103031
[37] Groebner R J, Leonard A W, Snyder P B, Osborne T H, Maggi C F, Fenstermacher M E, Petty C C and Owen L W 2009 Progress towards a predictive model for pedestal height in DIII-D *Nucl. Fusion* **49** 085037
[38] Mordijck S 2020 Overview of density pedestal structure: role of fueling versus transport *Nucl. Fusion* **60** 082006
[39] Ham C J *et al* (The JET Contributors) 2021 Towards understanding reactor relevant tokamak pedestals *Nucl. Fusion* **61** 096013
[40] Huysmans G T A and Czarny O 2007 MHD stability in X-point geometry: simulation of ELMs *Nucl. Fusion* **47** 659–66
[41] Czarny O and Huysmans G 2008 Bézier surfaces and finite elements for MHD simulations *J. Comput. Phys.* **227** 7423–45
[42] Hoelzl M *et al* 2021 The JOREK non-linear extended MHD code and applications to large-scale instabilities and their control in magnetically confined fusion plasmas *Nucl. Fusion* **61** 065001
[43] Belli E A, Candy J, Meneghini O and Osborne T H 2014 Limitations of bootstrap current models *Plasma Phys. Control. Fusion* **56** 045006
[44] Belli E A and Candy J 2008 Kinetic calculation of neoclassical transport including self-consistent electron and impurity dynamics *Plasma Phys. Control. Fusion* **50** 095010
[45] Belli E A and Candy J 2012 Full linearized Fokker–Planck collisions in neoclassical transport simulations *Plasma Phys. Control. Fusion* **54** 015015
[46] Mikhailovskii A B, Huysmans G T A, Kerner W O K and Sharapov S E 1997 Optimization of computational MHD normal-mode analysis for tokamaks *Plasma Phys. Rep.* **23** 844–57
[47] Huysmans G T A 2005 ELMs: MHD instabilities at the transport barrier *Plasma Phys. Control. Fusion* **47** B165–78
[48] Beurskens M N A *et al* 2011 H-mode pedestal scaling in DIII-D, ASDEX Upgrade and JET *Phys. Plasmas* **18** 056120
[49] Havlíčková E, Harrison J, Lipschultz B, Fishpool G, Kirk A, Thornton A, Wischmeier M, Elmore S and Allan S 2015 SOLPS analysis of the MAST-U divertor with the effect of heating power and pumping on the access to detachment in the Super-x configuration *Plasma Phys. Control. Fusion* **57** 115001
[50] Kallenbach A, Asakura N, Kirk A, Korotkov A, Mahdavi M A, Mossessian D and Porter G D 2005 Multi-machine comparisons of H-mode separatrix densities and edge profile behaviour in the ITPA SOL and Divertor Physics Topical Group *J. Nucl. Mater.* **337–339** 381–5
[51] Frassinetti L *et al* 2021 Role of the separatrix density in the pedestal performance in deuterium low triangularity JET-ILW plasmas and comparison with JET-C *Nucl. Fusion* **61** 126054
[52] Frassinetti L *et al* 2019 Role of the pedestal position on the pedestal performance in AUG, JET-ILW and TCV and implications for ITER *Nucl. Fusion* **59** 076038
[53] Stefanikova E, Frassinetti L, Saarelma S, von Thun C P and Hillesheim J C (JET Contributors) 2021 Change in the pedestal stability between JET-C and JET-ILW low triangularity peeling-ballooning limited plasmas *Nucl. Fusion* **61** 026008
[54] Hatch D R, Kotschenreuther M, Mahajan S, Valanju P and Liu X 2017 A gyrokinetic perspective on the JET-ILW pedestal *Nucl. Fusion* **57** 036020
[55] Hatch D R *et al* 2019 Direct gyrokinetic comparison of pedestal transport in JET with carbon and ITER-like walls *Nucl. Fusion* **59** 086056
[56] Saarelma S, Frassinetti L, Bilkova P, Challis C D, Chankin A, Fridström R, Garzotti L, Horvath L and Maggi C F 2019 Self-consistent pedestal prediction for JET-ILW in preparation of the DT campaign *Phys. Plasmas* **26** 072501
[57] Saarelma S, Hender T C, Kirk A, Meyer H and Wilson H R (MAST Team) 2007 MHD stability analysis of ELMs in MAST *Plasma Phys. Control. Fusion* **49** 31–42